Weather and Climate Extremes 45 (2024) 100703

Contents lists available at ScienceDirect

Weather and Climate Extremes

journal homepage: www.elsevier.com/locate/wace

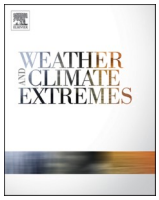

# Examining the role of biophysical feedbacks on simulated temperature extremes during the Tinderbox Drought and Black Summer bushfires in southeast Australia

Mengyuan Mu [a,b,*], Manon E.B. Sabot [a,b,c], Anna M. Ukkola [a,b], Sami W. Rifai [d], Martin G. De Kauwe [e], Sanaa Hobeichi [a,b,f], Andy J. Pitman [a,b]

[a] Climate Change Research Centre, University of New South Wales, Sydney, NSW, Australia
[b] ARC Centre of Excellence for Climate Extremes, University of New South Wales, Sydney, NSW, Australia
[c] Max Planck Institute for Biogeochemistry, Jena, Germany
[d] School of Biological Sciences, University of Adelaide, Adelaide, SA, Australia
[e] School of Biological Sciences, University of Bristol, Bristol, UK
[f] UNSW Data Science Hub and UNSW AI Institute, University of New South Wales, Sydney, NSW, Australia

ARTICLE INFO

*Keywords:*
Drought
Leaf area index
Albedo
Temperature extreme
Bushfire

ABSTRACT

The Tinderbox Drought (2017–2019) was one of the most severe droughts recorded in Australia. The extreme summer air temperatures (>40 °C) combined with drought, contributed to the unprecedented Black Summer bushfires in 2019–20 over southeast Australia. Whilst the temperature extremes were largely driven by synoptic processes, it is important to understand to what extent interactions between land and atmosphere played a role. In this study, we use the WRF-LIS-CABLE land-atmosphere coupled model to examine the impacts of changes in leaf area index (LAI) and albedo by contrasting simulations with climatological and time-varying LAI and albedo. We analyse the impact of these biophysical feedbacks on temperature extremes and fire risk during the Tinderbox Drought and the Black Summer bushfires. Remote-sensing data showed a decrease in LAI (0.1–4.0 $m^2$ $m^{-2}$) over the three years of the drought along the southeast coast of Australia relative to the long-term climatology, while albedo increased inland (0.02–0.14). These changes in LAI and albedo were accompanied by an overall decrease in daily maximum temperature ($T_{max}$) in the vast majority of interior regions (by ~0.5 °C) and, in the 2019–20 summer, by a clear increase in $T_{max}$ in the coastal regions of up to ~1 °C. Increased albedo explained most of the decreases in $T_{max}$ inland, whereas increases in $T_{max}$ along the coasts were mostly associated with LAI declines. The magnitude of the impact of biophysical changes on temperature demonstrates the potential impact that would be missed in simulations that assumed fixed vegetation properties. Finally, we only found a small impact from LAI and albedo changes on the fire risk (as measured by the fuel moisture index) preceding the Black Summer bushfires, suggesting these biophysical feedbacks did not significantly modulate fire risk. Our results have implications for coupled simulations relying on climatological LAI and albedo, including operation weather and seasonal climate predictions.

## 1. Introduction

The Tinderbox Drought, which began in 2017 and extended into early 2020, stands out as one of the most severe droughts in Australia's instrumental history (Abram et al., 2021; Bureau of Meteorology, 2020a; Nguyen et al., 2021). This drought primarily affected the southeast of Australia, including the Murray–Darling Basin which accounts for over 40% of national agricultural production. Years 2017–2019 were the driest 3-year period on record in eastern Australia (Nguyen et al., 2021) with 12 consecutive months with below average rainfall in the Murray–Darling region and strong rainfall declines experienced in particular during the cool season (April–September) (King et al., 2020). The Tinderbox Drought led to an estimated $AUD 53 billion total economic losses (Wittwer and Waschik, 2021) and threatened the water supply of the country's second largest city, Sydney (Sydney Water, 2020), and that of multiple rural towns (NSW DPI, 2020).

* Corresponding author. Climate Change Research Centre, University of New South Wales, Sydney, NSW, Australia.
*E-mail address:* mengyuan.mu@unsw.edu.au (M. Mu).

https://doi.org/10.1016/j.wace.2024.100703
Received 14 December 2023; Received in revised form 9 May 2024; Accepted 10 June 2024
Available online 11 June 2024

The drought was accompanied by extremely hot summers. The summers of 2018–2019 and 2019–2020 were the hottest on record in Australia, with the 2018–2019 summer setting a new national record, 0.86 °C higher than the previous record (Bureau of Meteorology, 2019). December 2019 experienced 11 days with an average daily maximum temperature ($T_{max}$) exceeding 40 °C on average nation-wide, a remarkable occurrence given only 11 days ≥ 40 °C had previously been recorded since 1910 (Bureau of Meteorology, 2020b). Southeast Australia was particularly hard hit by these heat extremes. In the 2018–2019 summer, temperatures in New South Wales broke previous records by up to 2 °C (Bureau of Meteorology, 2019). These heat extremes were caused by a combination of factors including anomalous synoptic processes and the very dry land surfaces caused by the ongoing multi-year drought, which likely intensified the heat extremes via the positive land–atmosphere feedback (Hirsch et al., 2019a; Miralles et al., 2019; Schumacher et al., 2019).

With co-occurring drought, low atmospheric relative humidity, extremely hot weather (Deb et al., 2020) and dry soils, combined with low moisture in dead and live fuels, the 2019–2020 Australian bushfire season (known as Black Summer) was the most destructive on record. The fire season started in early September 2019, spread across wide areas of southeast Australia and was unprecedented in its scale, severity, and impact (Abram et al., 2021; Filkov et al., 2020). The fires burned more than 5.8 million hectares of forest, including 21% of the Australia's temperate forests (Abram et al., 2021; Boer et al., 2020; Deb et al., 2020). The Black Summer bushfires released very large quantities of $CO_2$ into the atmosphere; estimates include 350 million tons between November and December (Sanderson and Fisher, 2020) and between 414 and 866 million tons for the drought- and fire-affected 2019–2020 growing season (Byrne et al., 2021). The fires claimed 28 human lives (Roach, 2020) and destroyed more than 3 000 houses (Wittwer and Waschik, 2021).

Drought stress can affect vegetation composition, structure and function (Gupta et al., 2020; Jiao et al., 2020; Nolan et al., 2021; Peters et al., 2018), and lead to crown die-back/tree mortality (Bréda et al., 2006; De Kauwe et al., 2022; Nolan et al., 2021) and reduced crop yield (Boyer et al., 2013; Stahl et al., 2016; van Dijk et al., 2013). At regional scales, the impact of drought can be tracked using satellite data to monitor reductions in leaf biomass (e.g. leaf area index; LAI) and fluctuation in surface albedo. Overall, the changes in LAI and albedo induced by both drought and fire should influence both surface energy balance and the coupled land-atmosphere system. Reductions in LAI modify the water and energy fluxes over land (Duveiller et al., 2018; Forzieri et al., 2020; Launiainen et al., 2019), while increases in surface albedo reduce the net radiation available to the surface energy balance and subsequently temperature (Graf et al., 2023; Li et al., 2015; Su et al., 2023; Wu et al., 2021), potentially altering regional precipitation (Sooraj et al., 2019; Terray et al., 2018). Thus, changes in either the amount of energy available at the surface (albedo) or the partitioning of energy into sensible versus latent heat fluxes (LAI) subsequently affect the risk of heat extremes, and the characteristics of the atmospheric boundary layer. Previous modelling work suggests that changes in key biophysical properties of the vegetated land surface (e.g. vegetation fraction and albedo) intensified the Millennium Drought that affected much of eastern Australia between 2001 and 2009 (Evans et al., 2017; Meng et al., 2014a, 2014b). Other model studies have also shown that using time-varying LAI and albedo rather than climatology can enhance model performance by improving simulated water and energy fluxes and increase potential predictability of temperature extremes (Boussetta et al., 2013, 2015; Duveiller et al., 2023; Koster and Walker, 2015; Nogueira et al., 2020; Ruiz-Vásquez et al., 2022, 2023). Some previous studies have also assimilated remotely-sensed observations into coupled weather and climate models to reflect how drought impacts the land surface (Boussetta et al., 2013, 2015; Ruiz-Vásquez et al., 2022, 2023; Yan et al., 2020). The updated vegetation (LAI, vegetation fraction, land cover) and albedo information enable these coupled models to better capture the near surface temperature forecasts (Alessandri et al., 2017; Boussetta et al., 2013, 2015; Knote et al., 2009; Liu and Chen, 2024; Yan et al., 2020). Boussetta et al. (2015) assimilated the near-real time LAI and surface albedo into the European Centre of Medium-Range Weather Forecasts (ECMWF) Integrated Forecasting System (IFS) and improved the detection of extreme events in regions with significant LAI and albedo anomalies, also reducing the errors in near-surface air temperature simulations. Further, Alessandri et al. (2017) introduced dynamic LAI observations into the ECMWF EC-Earth Earth System Model and found significant improvements in the forecast of 2-m temperature and rainfall over transitional land surfaces on seasonal to decadal timescales.

While both LAI and albedo influence the surface and the boundary layer, the nature, evolution and magnitude of this influence over sequential drought years is not clear, including the contribution these made to the remarkably hot summers experienced during the Tinderbox Drought and to the Black Summer bushfires. This lack of clarity has implications for our understanding of these extreme events but also for modelling applications as many regional simulations of weather and climate, including operational seasonal predictions in Australia, are forced with climatological LAI and albedo using a pre-determined seasonal cycle that does not incorporate the dynamic effects of drought or other disturbances on the vegetation. This study aims to advance our understanding of what impact dynamical changes in LAI and albedo had on temperature extremes and fire risk during the Tinderbox Drought and seeks to examine what impacts this has in typical simulations omitting this feedback. We use a land-atmosphere coupled model and simulations driven by climatological and observed (time-varying) LAI and albedo. Specifically, we explore whether the changes in LAI and albedo observed throughout the drought contributed to the remarkably hot summers in the last two years of the Tinderbox Droughts and whether these changes made conditions more conducive to the Black Summer bushfires.

## 2. Methods

### 2.1. Modelling system

We use the land-atmosphere coupled modelling system WRF-LIS-CABLE, which combines the National Aeronautics and Space Administration (NASA) Unified Weather Research and Forecasting (WRF) model version 9.2 (NU-WRF v9.2), a regional atmospheric model, with the Community Atmosphere–Biosphere Land Exchange (CABLE) land surface model (LSM). NU-WRF v9.2 incorporates the versions 3.9.1 of WRF and 7.2 of the Land Information System model framework (LIS), the latter which couples the atmospheric and land surface models. The CABLE LSM coupled to NU-WRF is based on CABLE 2.0 but with a new hydrology scheme developed by Decker (2015) and Decker et al. (2017).

The WRF atmospheric physics configurations follow Hirsch and King (2020) who selected a model configuration that performed well in simulating heat extremes over Australia, particularly for the summer months. These atmospheric configurations include the Mellor-Yamada-Janjic boundary layer and surface layer schemes, the New Tiedtke cumulus convection scheme, the RRTMG shortwave and longwave radiation schemes and the WRF Single-Moment 5-class microphysics scheme. Our simulation domain covers southeast Australia (Fig. 1a), including the states of New South Wales (NSW), Victoria (VIC), southern Queensland (QLD), and eastern South Australia (SA), as well as the Australian Capital Territory (ACT). A spatial resolution of 4 km is employed in the simulations in order to explore the impact of albedo and LAI on conditioning the landscape for fires.

The CABLE version within WRF-LIS-CABLE is extended from CABLE version 2.0, with the addition of subgrid-scale soil moisture, infiltration excess and saturation runoff generation mechanisms, as well as a dynamic unconfined groundwater aquifer beneath the 4.6 m soil column (Decker, 2015; Decker et al., 2017; Mu et al., 2021a). This version of CABLE has been evaluated extensively at both site- and global-scales and has shown good performance in simulating land water and energy fluxes

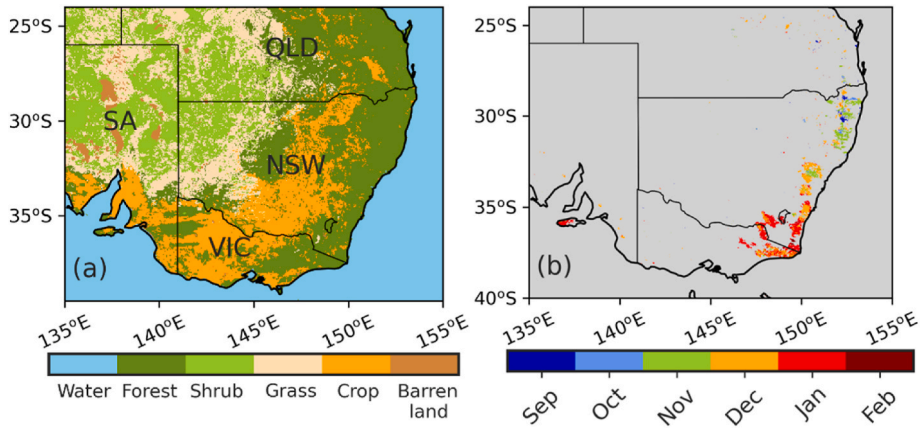


**Fig. 1.** (a) The map of land cover types over the studied region and (b) the extent of the Black Summer bushfires and month the fire started (September to December are in 2019 and January and February in 2020). In panel a, "forest" refers to broadleaf evergreen forest. The labels indicate Australian states: New South Wales (NSW), Victoria (VIC), Queensland (QLD) and South Australia (SA).

under both average and extreme conditions, including during the Tinderbox Drought period (Decker, 2015; Decker et al., 2017; Mu et al., 2021a, 2021b; Ukkola et al., 2016).

We evaluated WRF-LIS-CABLE using the Australian Gridded Climate Data (AGCD) observations (Jones et al., 2009). We found that the model (using ERA5) tends to underestimate $T_{max}$ by up to 4 °C, consistent with previous studies using ERA Interim (Hirsch et al., 2019b; Mu et al., 2022) (details in Supplementary Material). The underestimation of $T_{max}$ is mainly associated with an apparent cold bias in the ERA5 (and ERA Interim) reanalysis over the study region. However, as demonstrated by Mu et al. (2022) WRF-LIS-CABLE system also tends to underpredict the range of the diurnal temperature variation.

### 2.2. Experiment design

We first undertake a 137-year spin-up of the offline CABLE LSM following the approach of Mu et al. (2022). This spin-up includes 90 years of simulation with $CO_2$ concentrations fixed at the 1969 levels, recycling years 1970–1999 from the Australian Gridded Climate Data (AGCD) meteorology forcing dataset (Jones et al., 2009). We then run the model for 1970–2016 using time-evolving $CO_2$ and time-varying AGCD meteorological dataset to derive initial conditions for soil moisture and groundwater aquifer moisture for the coupled experiments using WRF-LIS-CABLE. The coupled simulations were then run from January 1, 2017 to February 29, 2020, forced at the boundaries by the European Centre for Medium-Range Weather Forecasts (ECMWF) Reanalysis v5 (ERA5; Hersbach et al., 2020). We note that we do not use nested domains to transition from the 31 km ERA5 atmospheric forcing to the 4 km simulations conducted here. This was a compromise between the computational costs of these simulations, and the desire to resolve terrestrial processes at very high spatial detail, which does not limit our ability to evaluate the effects of prescribed changes in land properties on near-surface temperature.

We undertake two experiments to examine the impact of drought-associated changes in LAI and albedo. The first experiment uses climatological daily LAI and albedo calculated using remotely-sensed observations for 2003–2022 (Clim) (see Section 2.3). The second experiment uses time-varying daily LAI and albedo observations (Dyn) and therefore captures the LAI and albedo changes associated with the drought and fire events. Due to the high computational cost of running WRF-LIS-CABLE at 4 km resolution for a period of ~3 years, we only run one simulation for each experiment.

### 2.3. Datasets

We use the ERA5 dataset to drive the boundary conditions of the WRF-LIS-CABLE coupled model. This dataset is at a horizontal resolution of 31 km and an hourly temporal resolution. The ERA5 dataset has been widely used in climate analyses (Chiodi et al., 2021; Fang et al., 2022; Zscheischler et al., 2021), model evaluations (Ajjur and Al-Ghamdi, 2021; Tarek et al., 2020) and for driving regional and global climate models (Segura et al., 2021; Wei et al., 2021).

The land cover type in our simulations is sourced from the National Dynamic Land Cover Data of Australia (DLCD) dataset (https://www.ga.gov.au/scientific-topics/earth-obs/accessing-satellite-imagery/landcover, last access: August 29, 2021), which is aggregated to five plant functional types (PFTs) used by CABLE as shown in Fig. 1a (see Mu et al., 2021b). The soil hydraulic parameters are derived using the Cosby pedotransfer functions (Cosby et al., 1984) and the SoilGrids soil properties maps (Hengl et al., 2017), which provide the fraction of sand, clay, silt, and organic carbon at six depths, from the soil surface down to 2 m. We weight the SoilGrids depth-varying soil properties to match the depth of model soil layers and the groundwater aquifer and assume the soil properties below 2 m equal those in SoilGrids at 2 m. These soil properties are then used to calculate depth-varying soil hydraulic parameters for the CABLE soil layers and groundwater aquifer.

We use version 6.1 of the Moderate Resolution Imaging Spectroradiometer (MODIS) to estimate the climatology and time-varying LAI and albedo used in our simulations during the periods of Tinderbox Drought. The LAI data is from the MCD15A3H MODIS product, which combines the measurements from Terra and Aqua satellites to create a 4-day composite dataset at 500 m spatial resolution (Myneni et al., 2021). The albedo is from the Bidirectional Reflectance Distribution Function and Albedo (MCD43C3) product, which uses the 16-day Terra and Aqua MODIS data to provide the 8-day data at a 0.05° (~5 km) spatial resolution (Schaaf and Wang, 2021). The albedo used in the simulations includes black sky albedo and white sky albedo for the visible and near-infrared bands. Both the albedo and LAI dataset were extracted using the Google Earth Engine (https://developers.google.com/earth-engine/datasets/catalog/MODIS_061_MCD15A3H; last access March 16, 2023). We fill the missing observations by carrying the last observation forward in time, then aggregate to a weekly resolution, and smooth the timeseries with a weighted Whittaker filter using a second order finite difference penalty. The dataset is finally linearly interpolated into daily resolution and to the 4 km WRF domain with the nearest-neighbor interpolation to drive the model. The period of January 1, 2003 to December 31, 2022 is used to calculate the daily climatology.

To analyse the impact of the Black Summer bushfires on the LAI and albedo, we use version 6.1 of MODIS Global Burned Area Product (MCD64A1) product at a 500-m spatial resolution to identify burned areas and the date the fire commenced at each location

(Fig. 1b–Boschetti et al., 2019; Giglio et al., 2018). This dataset provides similar spatial and temporal patterns of the Black Summer bushfires burned regions as the Fire Extent and Severity Mapping product (FESM, https://datasets.seed.nsw.gov.au/dataset/fire-extent-and-severity-mapping-fesm, last access: December 14, 2023) and the Google Earth Engine Burnt Area Map (GEEBAM, https://datasets.seed.nsw.gov.au/dataset/google-earth-engine-burnt-area-map-geebam, last access: December 14, 2023).

### 2.4. Fuel moisture index

To determine the potential impact of changes in LAI and albedo on fire risk in the lead-up to the Black Summer, we calculated the Fuel Moisture Index (FMI, Sharples and McRae, 2011), which assesses the dead fuel moisture content:

$$FMI = 10 - 0.25\,(T - q)$$

where $T$ (°C) is the air temperature and $q$ (%) is the relative humidity. A lower FMI is taken as a proxy for drier fuel and a higher fire risk. While the FMI does not consider the impact of fuel quantity and type of fuel, it provides a general climatological estimate of likely fuel dryness in conditions conducive to extreme fires (Abram et al., 2021; Sharples and McRae, 2011).

## 3. Results

### 3.1. Temperature differences during the tinderbox drought and black summer

We first contrast the evolution of daily near-surface maximum temperatures ($T_{max}$) during the three-year Tinderbox Drought in the Dyn and Clim simulations designed to quantify the impact of biophysical feedback (LAI and albedo) on the atmosphere. Fig. 2 shows $T_{max}$ differences ($\Delta T_{max}$, Dyn – Clim) over the three years of drought. Overall, the use of time-varying LAI and albedo led to differences of up to 0.7 °C during the Tinderbox Drought, especially from the winter of 2018 onwards, albeit with notable variations across seasons and space. In the inland regions, $T_{max}$ differences generally evolved from positive $\Delta T_{max}$ of 0.1–0.4 °C at the start of the drought (Fig. 2a) to negative $\Delta T_{max}$ of 0.1–0.7 °C in the last year of the drought (Fig. 2e). The higher $T_{max}$ in

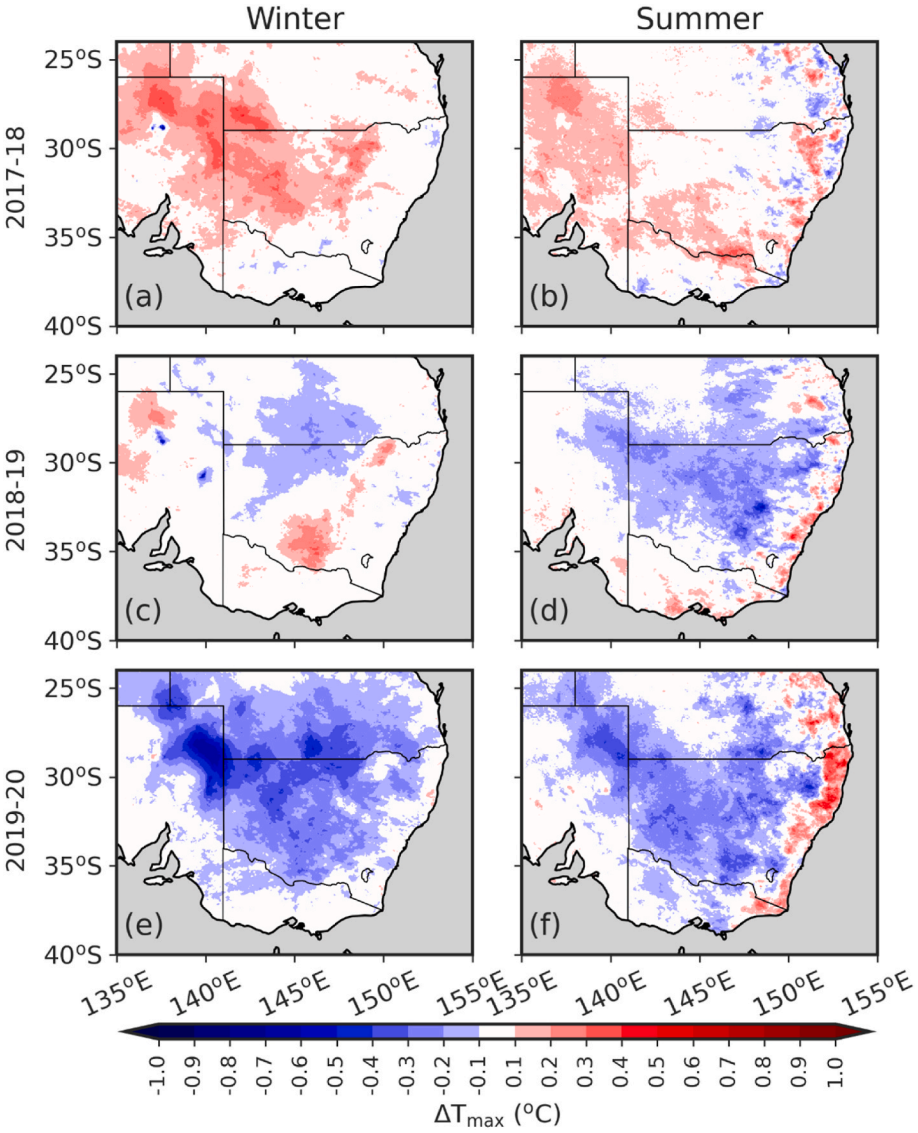


**Fig. 2.** The $T_{max}$ difference ($\Delta T_{max}$, °C) between Dyn and Clim through the three years of the Tinderbox Drought. The left column refers to winters (June–August) and the right column to summers (December–February). The top row is for the 2017 winter (a) and 2017–18 summer (b), the second row for the 2018 winter (c) and 2018–19 summer (d), and the third row for the 2019 winter (e) and 2019–20 summer (f).

Dyn compared to Clim at the start of the drought was evident in the western parts of the domain but weakened within the first year of the drought. By the winter 2018, the differences were smaller and more varied with both negative and positive $\Delta T_{max}$ in the inland regions (Fig. 2c). In the summer of 2018–19 (Fig. 2d), cooler temperatures were simulated in Dyn across the areas that were most strongly impacted by the drought (in particular inland NSW). The negative $\Delta T_{max}$ intensified and spread across much of the model domain in the following winter (Fig. 2e), and largely persisted into the following summer. The $T_{max}$ differences along the coast were less consistent and mostly negligible during winter (Fig. 2a, c, 2e). Both negative and positive differences arose during the first two summers of the drought (Fig. 2b and d). During the last summer of the drought (2019–20), $\Delta T_{max}$ was consistently positive across large parts of the eastern coast (Fig. 2f). $T_{max}$ differences were particularly high (by up to 0.6 °C) between the latitudes of 28–38°S which were areas strongly affected by the Black Summer bushfires.

We further explore the 2019–20 summer period as this is when we see some of the largest differences in $T_{max}$ from using time-varying LAI and albedo (i.e., an inland cooling of $T_{max}$ contrasting a coastal increase in $T_{max}$). This is also when the Tinderbox Drought reached its peak intensity, culminating in the Black Summer bushfires. Fig. 3a–c shows the monthly evolution of $T_{max}$ differences between December 2019 and February 2020. Positive $\Delta T_{max}$ (~0.5 °C) were largely isolated to northern NSW (~30°S) in December 2019 but grew in area and intensity to affect most of the eastern coastal region by January 2020 (locally reaching about 1 °C difference) and then propagated westward by February 2020. These regions broadly correspond to the regions affected by the bushfires (cf. Fig. 1b).

To show how these temperature differences also affected the atmosphere, we examine the vertical profile of the differences in daily maximum potential temperature ($\Delta\theta_{max}$) for the transects (see Fig. 3a–c dashed lines) taken across the northern (30°S), central (33°S), and southern (37.5°S) fire-affected regions. These transects show that the temperature changes were not isolated to the near-surface but extended throughout the atmospheric boundary layer. These $\Delta\theta_{max}$ were closely associated with the corresponding albedo and LAI differences along each transect (see the horizontal inserts at the bottom of panels d–l in Fig. 3), such that strong positive $\Delta\theta_{max}$ through the lower 1 500 m of the atmosphere tended to coincide with areas where LAI was lower in Dyn compared to Clim, whereas strong negative $\Delta\theta_{max}$ extending as high as 3 000 m primarily coincided with higher albedo in Dyn compared to Clim. Overall, using observed changes in albedo and LAI affected the surface energy balance but, near the coast, also heated the lower atmosphere by up to ~0.7 °C, with the potential to affect subsequent temperatures via heat recycling (cf. Miralles et al., 2014).

### 3.2. Impacts of LAI and albedo on the temperature differences

Beyond changes to LAI and albedo during the summer of 2019–20 and along the three transects discussed above, the three years of the

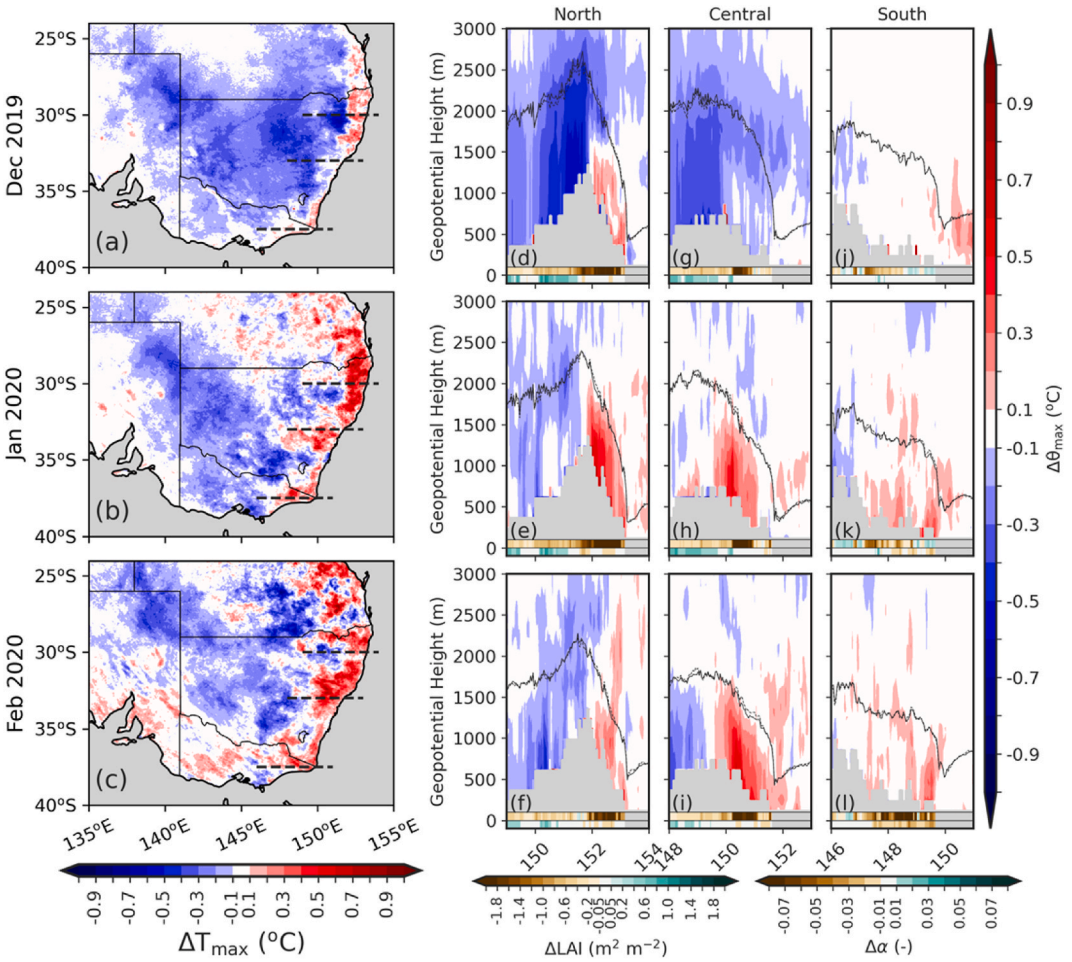


**Fig. 3.** The difference in $T_{max}$ ($\Delta T_{max}$, °C, 1st column) and in atmospheric maximum potential temperature ($\Delta\theta_{max}$, °C, 2nd –4th columns) between Dyn and Clim. The first row is for December 2019, the second row for January 2020, and the third row for February 2020. The 2nd, 3rd and 4th columns are, respectively, for the North (~30°S), Central (~33°S) and South (~37.5°S) transects indicated by the three dashed lines shown in each panel of the first column. The changes in LAI and albedo between Dyn and Clim are shown in insets within each of the subpanels in the 2nd – 4th columns, with the change in LAI ($\Delta$LAI, $m^2\ m^{-2}$) displayed above the change in albedo ($\Delta\alpha$, unitless).

Tinderbox Drought saw large-scale regional variations in LAI and albedo which are not captured by model simulations that use fixed climatological biophysics. We next analyse the evolution of LAI and albedo during the drought before disentangling their effect on the $T_{max}$ differences between Clim and Dyn. Figs. 4 and 5 show the LAI and albedo anomalies, respectively, relative to their climatology (i.e., Dyn−Clim) over the three years of the Tinderbox Drought.

In the inland regions, which are dominated by shrubs and grassland with crops in the southeastern parts (Fig. 1a), the drought initially induced localised LAI anomalies (ΔLAI) from $-1.0$ $m^2$ $m^{-2}$ to $+2.0$ $m^2$ $m^{-2}$ (Fig. 4a–b). This positive LAI anomaly may have resulted from unusually wet conditions in 2016 which encouraged an overall higher LAI than climatology at the beginning of the drought. As the drought progressed, the ΔLAI became largely negative in the winter of 2018 and was sustained for the remainder of the drought (Fig. 4c–f), apart from some southern and northern regions in the 2019 winter (Fig. 4e). The albedo anomalies (Δα) were small overall during the first year of the drought (Fig. 5a–b), except for negative anomalies in the northwestern parts of the domain. For the remainder of the drought, the Δα were positive across most of the inland regions, implying an increase in surface reflectance. The anomalies reached up to 0.08 compared to the climatology (for context, albedo are typically 0.05–0.2 for forests, 0.1–0.25 for grassland and cropland, and 0.2–0.45 for dry sandy soil; Dobos, 2005). Examining the $T_{max}$ differences in Fig. 2, the $\Delta T_{max}$ patterns seen in the inland regions are most consistent with the evolution of the albedo anomalies. The higher temperatures seen inland during the first year of the drought (Fig. 2a–b) spatially correspond to the regions of negative Δα that would increase the available net radiation. Conversely, Dyn shows lower temperatures (negative $\Delta T_{max}$) from winter 2018 onwards (Fig. 2c–f) which match closely to the areas of positive Δα (Fig. 5c–f) that would decrease net radiation. LAI, on the other hand, clearly declined during this period (from winter 2018 onwards), which is normally associated with higher rather than lower temperatures due to reduced evaporative cooling. However, the general decrease in $T_{max}$ suggests that temperature changes over this region are dominated by the albedo anomalies rather than the LAI anomalies. That is likely because both Dyn and Clim simulations had a dry root zone profile (Fig. 6j-6o), which limits evaporation and thus reduces the influence of LAI dynamics.

The coastal regions, which are dominated by broadleaf evergreen

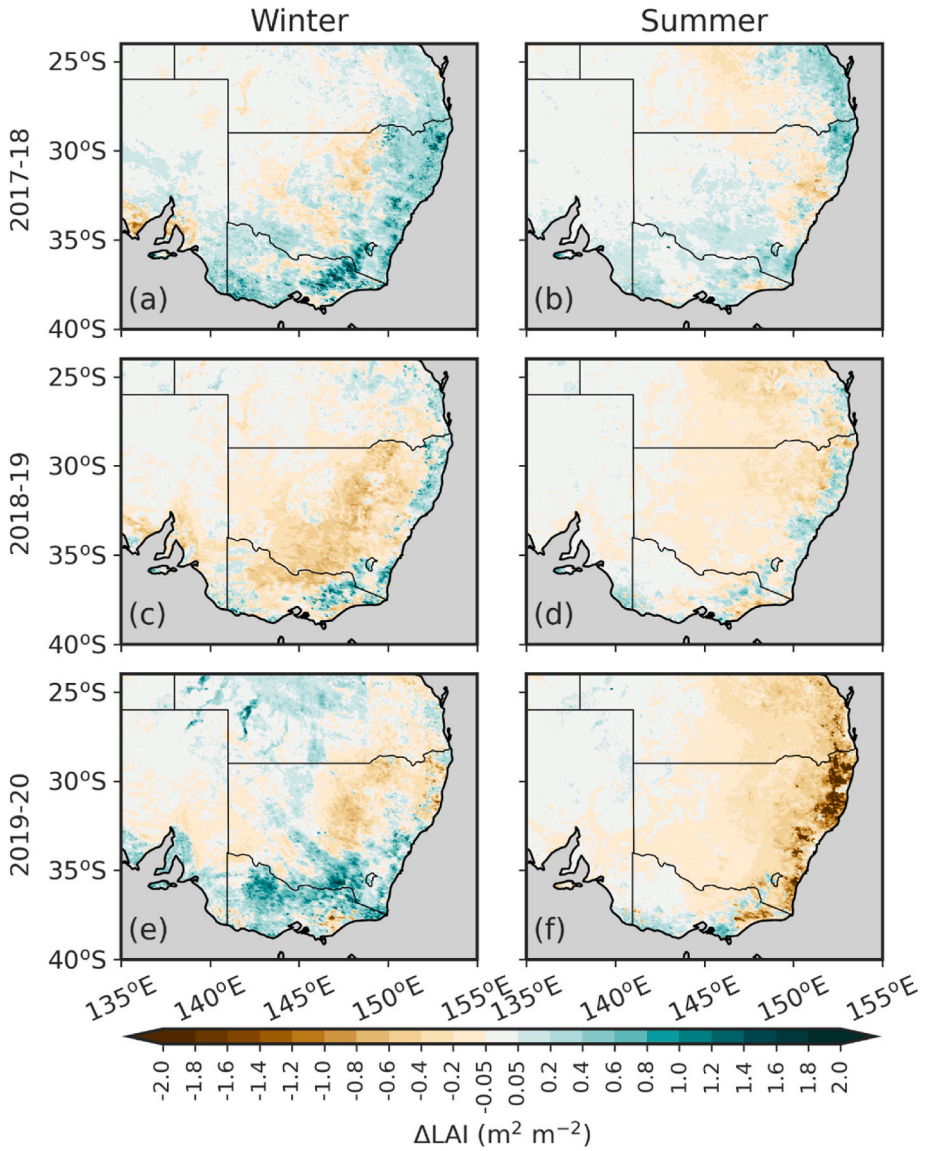


**Fig. 4.** The LAI difference (ΔLAI, $m^2$ $m^{-2}$) between Dyn and Clim through the three years of the Tinderbox Drought (left column: winter; right column: summer). The top row is for the 2017 winter (a) and 2017–18 summer (b), the second row for the 2018 winter (c) and 2018–19 summer (d), and the third row for the 2019 winter (e) and 2019–20 summer (f).

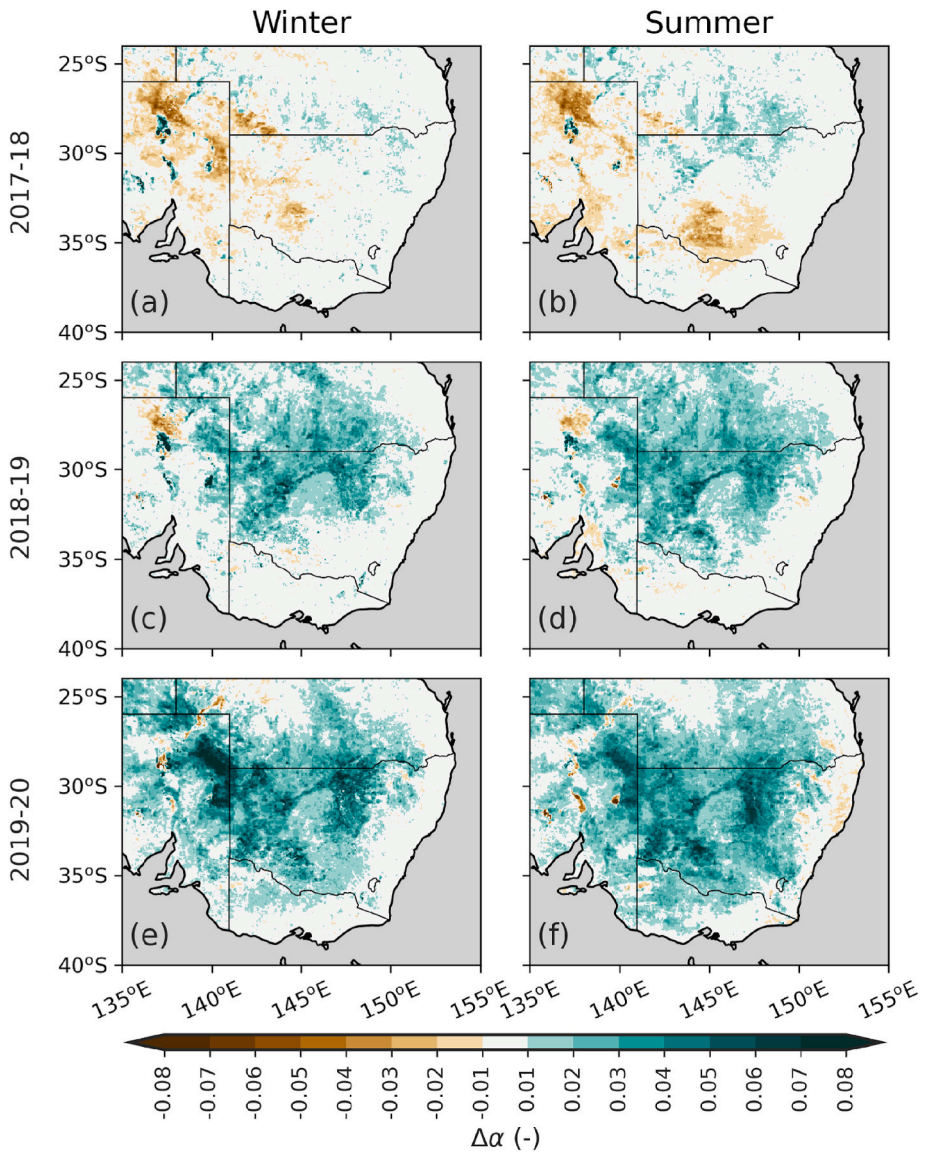


**Fig. 5.** The albedo difference (Δα, unitless) between Dyn and Clim through the three years of the Tinderbox Drought (left column: winter; right column: summer). The top row is for the 2017 winter (a) and 2017–18 summer (b), the second row for the 2018 winter (c) and 2018–19 summer (d), and the third row for the 2019 winter (e) and 2019–20 summer (f).

forests (Eucalyptus sp.) (Fig. 1a) showed a very different temporal evolution in LAI and albedo compared to the inland regions. Much of the coast showed positive ΔLAI of up to 1.6 $m^2$ $m^{-2}$ at the start of the drought (Fig. 4a). These anomalies weakened as the drought progressed, with some coastal regions showing negative anomalies (Fig. 4e–f). However, these were not sustained through the three years of the drought, with the location of stronger anomalies shifting each season (Fig. 4b–e). As the drought peaked, and the Black Summer bushfires swept through large parts of the eastern coast during the summer of 2019–20, negative ΔLAI of up to 2.0 $m^2$ $m^{-2}$ were observed (Fig. 4f). The negative anomalies were most pronounced in the regions affected by fires, in particular around 28–37°S, but even outside these regions the LAI on the eastern coast was consistently below climatological averages during this period. Conversely, the albedo showed few changes compared to the climatological conditions along the coastal regions during the three years of the drought (Fig. 5). Except some localised anomalies, Δα was largely within 0.01 of the long-term average. Taken together, these anomalies suggest that the $T_{max}$ differences between Dyn and Clim along the coast (Fig. 2) were largely driven by LAI (and differences in evaporation) rather than albedo changes. While $\Delta T_{max}$ and ΔLAI were fairly localised during most of the drought, in the summer of 2019–20, $\Delta T_{max}$ was strongly positive along much of the eastern coast (Fig. 2f), consistent with the observed strong reduction in LAI (Fig. 4f).

### 3.3. *Impacts of LAI and albedo changes on the surface energy and water balance*

To further disentangle the relationships between $T_{max}$, LAI and albedo, we analyse the conditions during the extremely hot summer periods of the Tinderbox Drought. Specifically, we compare the $\Delta T_{max}$ with the associated differences in net radiation ($\Delta R_{net}$) and latent heat flux (ΔLH), as well as the ratios of actual soil moisture content to saturated soil moisture content in the top 0.5 m ($\theta_{0.5m}/\theta_{sat,0.5m}$) to understand how LAI and albedo anomalies changed the surface energy and water balance over land and influenced the extremely hot summers in the Tinderbox Drought (Fig. 6).

In the 2017–18 summer, the $\Delta T_{max}$ (Fig. 6a) were not spatially coherent but they were associated with positive $\Delta R_{net}$ (Fig. 6d) of ~2–18 W $m^{-2}$ over the croplands in the southern central area of the domain, consistent with the albedo anomalies shown in Fig. 5b. There

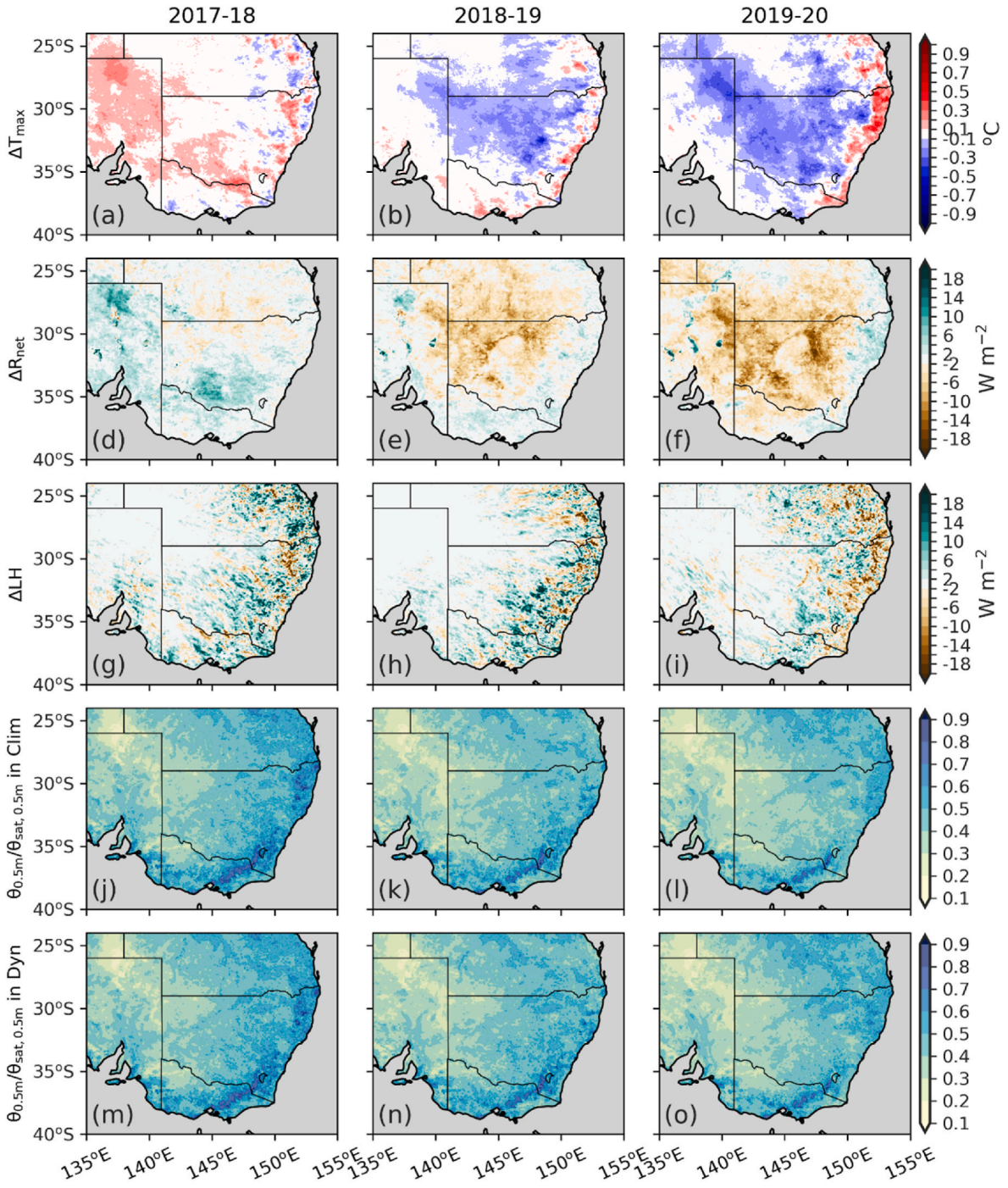


**Fig. 6.** The differences (Dyn − Clim) in $T_{max}$ ($\Delta T_{max}$, °C, panels a–c), $R_{net}$ ($\Delta R_{net}$, W m$^{-2}$, panels d–f), and LH (ΔLH, W m$^{-2}$, panels g–i), as well as the ratios of actual soil moisture content to saturated soil moisture content in the top 0.5 m ($\theta_{0.5m}/\theta_{sat,0.5m}$) in Clim (panels j–l) and Dyn (panels m–o) in the summers of the Tinderbox Drought. The first column refers to the 2017–18 summer, the second to the 2018–19 summer, and the third to the 2019–20 summer.

was also an association between local $\Delta T_{max}$ and ΔLH (Fig. 6g), with local reductions in LH (i.e., negative ΔLH) leading to positive $\Delta T_{max}$ (Fig. 6a). These changes were not strongly associated with changes in soil moisture (Fig. 6j, m). In the summer of 2018–19, Fig. 6b shows widespread negative $\Delta T_{max}$ in inland areas, and localized positive $T_{max}$ differences near the coast. The negative $\Delta T_{max}$ were associated with negative $\Delta R_{net}$ by −2 to −18 W m$^{-2}$ (Fig. 6e) which was clearly related to the albedo anomalies (Fig. 5d). In the 2019–20 summer, cooler $T_{max}$ (Fig. 6c) was simulated in Dyn compared to Clim in inland areas, resulting from the lower $R_{net}$ by 6–22 W m$^{-2}$ (Fig. 6f) which was associated with the positive albedo anomalies (Fig. 5f). However, along the forested coastal regions, although there were not widespread differences between Dyn and Clim in the summer of 2018–19 (Fig. 6b), $T_{max}$ was up to 0.7 °C higher in Dyn than in Clim in the 2019–20 summer (Fig. 6c). $R_{net}$ was locally 2–14 W m$^{-2}$ higher (Fig. 6f), and ΔLH reduced by up to 20 W m$^{-2}$ near the coasts, associated with the significant LAI decline (Fig. 4f).

Fig. 6j–o shows the ratio of actual soil moisture content to saturated moisture content in the top 0.5 m of soil for Clim and Dyn. Both model simulations show a drying trend of the root zone (i.e. the top 0.5 m soil, where most roots grow) extending from inland to the coast throughout the drought. The extremely dry conditions inland likely limited the

impact from changing LAI on LH and therefore on the $T_{max}$ differences. However, the generally wetter soils near to the coast allowed the LAI anomalies in the 2019–20 summer to reduce LH and increase $T_{max}$ in Dyn relative to Clim.

The differences in $R_{net}$ alone could not fully explain the emergence of the positive $\Delta T_{max}$ along the coastal regions in the summer of 2018–19 (Fig. 6b) and their significant intensification during the 2019–20 summer (Fig. 6c). A somewhat equivocal pattern of negative ΔLH began to develop in the summer of 2018–19 (Fig. 6h), becoming clearer and more widespread by the summer of 2019–20 (Fig. 6i), especially in regions of greater tree cover (i.e. along the eastern coast). The differences in LH exceeded 10–20 W $m^{-2}$ and were not strongly associated with

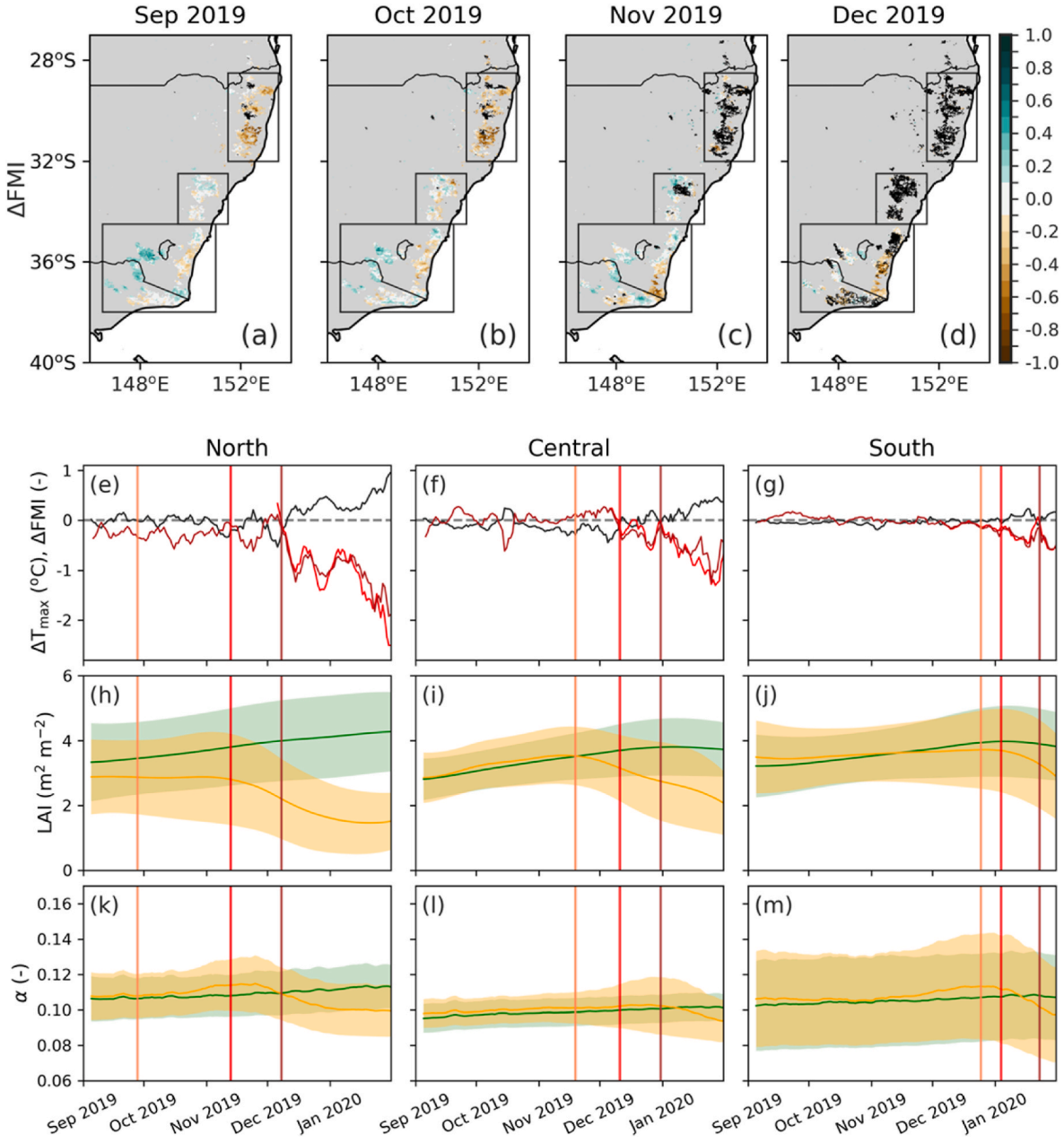


**Fig. 7.** Spatial map and time series of the regions burned during the Black Summer bushfires. Panel a–d are the differences (Dyn − Clim) in daytime FMI (ΔFMI, unitless) from September to December 2019. The three boxes in each panel highlights the north (28.5–32°S, 151.5–153.5°E), central (32.5–34.5°S, 149.5–151.5°E) and south (34.5–38°S, 146.5–151°E) burned regions. Panels e–g are the time series of the differences (Dyn − Clim) in $T_{max}$ ($\Delta T_{max}$, °C; black line) and FMI (ΔFMI, unitless; red lines). The dark red line refers to daytime ΔFMI, which is calculated from the 6-h simulation outputs (i.e. the time step of 10 a.m. and 4 p.m. are used), and the lighter red line refers to the daily maximum ΔFMI, which is calculated by $T_{max}$ and relative humidity when $T_{max}$ occurs from hourly output. Due to the computing and storage costs, we only put out the periods from December 2019 to February 2020 in hourly resolution, and the other simulated period is in 6-h resolution. The dashed horizontal line marks the zero line. Panels h–j are the time series of actual LAI (ΔLAI, $m^2$ $m^{-2}$), and panels k–m are actual albedo (Δα, unitless) over the fire season of September 2019 to January 2020. The North (left column), Central (middle column) and South (right column) burned regions are as shown in panel a–c. In panels h–m, the Clim and Dyn experiments are shown in green and orange solid lines, respectively, and the shadings around them are the uncertainty across pixels of one standard deviation. All timeseries are smoothed using a 5-day running window. The three vertical lines from left to right indicate the date when the fires had burnt 10% (orange), 50% (red), and 90% (brown) of the regions' total burnt area in the Black Summer bushfires. The simulations are interpolated to 500-m spatial resolution to match with the MODIS fire map. (For interpretation of the references to colour in this figure legend, the reader is referred to the Web version of this article.)

differences in soil moisture (see the lower two rows of Fig. 6). As the soil moisture does not appear to be limiting plant function along the coast, this suggests that ΔLH was driven by LAI differences between Dyn and Clim rather than soil moisture differences.

### 3.4. The impacts of LAI and albedo changes on fire risk

It is a reasonable hypothesis that the widespread declines in LAI induced increases in $T_{max}$ in the coastal regions in Dyn relative to Clim, hence worsening the projected fire risk. We examine the impact of the biophysical feedbacks on fire risk during the Black Summer bushfires by analysing changes in the FMI - an atmospheric proxy for dead fuel moisture content. Fig. 7a–d shows the difference in the FMI between Dyn and Clim for the pixels that eventually would burn during the Black Summer. The fires commenced in the northeastern regions in September and spread south as the fire season progressed. Fig. 7a and b shows that fire risk was higher in Dyn (i.e., ΔFMI was negative) during September–October in the northern regions, suggesting the temperature and/or humidity (i.e. LH) changes induced by a declining LAI increased the fire risk prior to these areas burning. The southern regions started burning in November but the impact of ΔLAI on the FMI is less consistent in this region, with both localised increases and decreases in the FMI in Dyn compared to Clim (Fig. 7c and d). As there were no strong Δα associated with the burnt regions (Fig. 5), we cannot conclude that local albedo feedbacks influenced fire risk. However, our simulations suggest that the fire risk was, to some extent, modulated by dynamic changes in LAI.

To further understand how the temperature and land properties changed in the lead up to fire, and after fire, we show the time series of $\Delta T_{max}$, ΔFMI, LAI and albedo from September 2019 to February 2020 for the three regions (Fig. 7e–m). The three vertical lines in each panel show the date when 10%, 50% and 90% of each of the three regions has combusted. In each region, $T_{max}$ begins to increase most clearly after 90% of the region has combusted and FMI declines coincided with this increase in $T_{max}$ (Fig. 7e, f, 7g). In the northern region, the zonally-averaged LAI clearly diverged before the fire started, supporting widespread drought impacts on LAI. This coincides with lower FMI and thus increasing fire risk in Dyn compared to Clim. In the other two regions, drought impacts on LAI were more heterogeneous as the zonally-averaged LAI only notably diverged once the fires had already burnt 10% of the central region (Figs. 7i) and 50% of the southern region (Fig. 7j). In all three regions, the albedo only declined after >50% (northern and southern region) to >90% (central regions) of the areas had burnt, likely reflecting a darkening of the surface from the fires. Overall, the biophysical effects we evaluated here only had a negligible impact on fire risk before the fires, except the northern region. Nevertheless, in all regions, the impact on $T_{max}$ and on the FMI increased after rapid declines in LAI from the onset of the fires. This suggests a potential for rapid LAI declines (induced by fire or other disturbances) to drive further temperature increases after the disturbances (e.g. post fires), a significant effect that would be missed in a simulation using climatological LAI and albedo.

## 4. Discussion and conclusions

In this study, we use the WRF-LIS-CABLE land-atmosphere coupled model to investigate the impact of LAI and albedo changes on the temperature extremes in southeast Australia's Tinderbox Drought and Black Summer bushfires. By contrasting the effects of climatological versus observed time-varying LAI and albedo, this study quantifies how important these commonly missing biophysical feedback is for simulations of maximum temperature and fire risk during drought. The time-varying albedo was higher at the interior of southeastern Australia during the Tinderbox drought compared to the climatology, while the time-varying LAI was lower near the coast. The increase in albedo caused up to a 0.7 °C decrease in maximum temperature inland, while the combined effects of LAI and albedo caused up to a 0.5 °C increase along the coasts in the 2019–20 summer before the fires. The primary reason for the maximum temperature changes inland was the change in albedo, which had the effect of reflecting more solar radiation into the atmosphere and thus reduced the surface net radiation. The mechanisms leading to increased $T_{max}$ near the coasts were more complicated. Drought- and fire-induced changes to LAI led to $T_{max}$ increasing by up to 1.2 °C at the surface and 0.6 °C in the atmospheric boundary layer in the regions burned in the Black Summer fires. In both cases, the temperature anomalies propagated into the atmosphere to impact the whole of the boundary layer.

The magnitude of the temperature changes linked to dynamic LAI and albedo are broadly comparable to previous studies. For example, Boussetta et al. (2015) found temperature increases of 0.1–1 °C from LAI and albedo changes that were of similar magnitude to this study using the European Centre for Medium Range Weather Forecasts integrated forecasting system. Similarly, Evans et al. (2017) and Meng et al. (2014a, 2014b) found temperature differences of 0.6–0.9 °C in WRF simulations ran with time-varying and climatological vegetation fraction (relatively linked to LAI) and/or albedo. These temperature changes suggest seasonal forecasts might be improved by representing time-varying LAI and albedo (Alessandri et al., 2017; Boussetta et al., 2015; Knote et al., 2009; Ruiz-Vásquez et al., 2022). However, we note the cold biases of 1∼4 °C in the simulated summer $T_{max}$ in both Dyn and Clim, which is very similar to a previous evaluation of WRF-LIS-CABLE undertaken using ERA Interim (Hirsch et al., 2019b). This cold bias would be worth examining further before using WRF-LIS-CABLE for predictions as distinct from model sensitivity studies.

We also explored how these changes in LAI and albedo affected the simulated conditions linked to the Black Summer bushfires. In our coupled model the time-varying LAI and albedo (Dyn) had a subtle effect on the FMI (<0.5 but up to 1.0 locally) before the fires, suggesting any biophysical feedbacks had a minor role in increasing fire risk. This is most likely because, in both sets of model simulations, the rootzone soil moisture is low (Fig. 6) which limits the impact of changes in LH (via reductions in LAI) on $T_{max}$. In effect, because we cannot validate the accuracy of the modelled soil moisture profiles (in particular their evolution in time), we cannot be sure if the correct biophysical feedbacks imposed by fixed vs dynamic LAI were captured. The land model we used may also fail to fully capture the impact of drought on the vegetation as it does not include representations of hydraulic damage and then failure, nor of plant root adaptation to drought (Gupta et al., 2020; Nolan et al., 2021), although these processes are now being integrated into land models (De Kauwe et al., 2020, 2022; Niu et al., 2020; Sabot et al., 2020, 2022). Nevertheless, by using a dynamic LAI forcing (Dyn), we do capture any emergent canopy dieback, in line with field-observations (Nolan et al., 2021).

Nevertheless, we show a strong effect on $T_{max}$ and FMI after the fires in the North and Central regions, with $T_{max}$ increases of up to 1 °C and FMI declines of up to −2. This demonstrates that a rapid disturbance in LAI and albedo, in this case induced by fire and drought, can have a significant impact on $T_{max}$ and FMI for the post-fire periods that would be missed in a simulation using fixed climatology.

We acknowledge specific limitations in our research. First, we base our analysis on the MODIS LAI product which have been shown to overestimate LAI over eastern Australian closed-canopy forest and woodlands sites (Leuning et al., 2005) and struggle to capture the impact of the vertical structure of savannas on LAI (Biudes et al., 2014; Fang et al., 2019; Hill et al., 2006; Mayr and Samimi, 2015). Although the assessments were carried out on earlier MODIS collections (4 vs 6) these issues may persist. Second, we only ran one ensemble of the regional climate model due to the computing resources and time required for the 3-year WRF simulations at 4 km resolution. This may impose a model limitation on our experiments by not considering the impact of initial conditions or different physics configurations. However, we anticipate the impact of ensembles would have a limited influence on our results, as the model configuration is widely evaluated and has been shown to

perform well and comparable to the previous ensemble mean over the studied region (Hirsch et al., 2019b; Hirsch and King, 2020).

Third, soil moisture dynamics plays a critical role in the evolution of drought-heat compound extremes (Miralles et al., 2019; Osman et al., 2022; Rasmijn et al., 2018; Seneviratne et al., 2010). While soil moisture assimilation can improve synoptic and seasonal weather forecasts (Dirmeyer and Halder, 2016; Dy and Fung, 2016; Zhang et al., 2020), the lack of real-time soil moisture observations over the root zone in our region made it impossible to consider in our model experiments.

In summary, our results highlight value in further developing the representation of the land surface in regional modelling. In Australia the Australian Community Climate Earth-System Simulator – Seasonal (ACCESS–S, Wedd et al., 2022) is used for multi-week to seasonal forecasts and uses monthly climatological LAI and albedo. The temperature, humidity and surface flux changes reported here by using remotely sensed LAI and albedo could enhance existing forecast systems relatively easily. Additionally, our study highlights that using remotely sensed time-varying LAI and albedo could lead to better forecasts of climate extreme events at a fine resolution. The temperature differences simulated between inland non-forest and coastal forest regions were particularly apparent during the severe drought period. This implies that to capture the spatial heterogeneity of temperature extremes during drought requires LAI and albedo anomalies to be taken into consideration.

## CRediT authorship contribution statement

**Mengyuan Mu:** Writing – review & editing, Writing – original draft, Visualization, Methodology, Investigation, Formal analysis, Data curation, Conceptualization. **Manon E.B. Sabot:** Writing – review & editing, Writing – original draft, Visualization, Methodology, Investigation, Formal analysis, Conceptualization. **Anna M. Ukkola:** Writing – review & editing, Writing – original draft, Visualization, Methodology, Investigation, Formal analysis, Conceptualization. **Sami W. Rifai:** Writing – review & editing, Writing – original draft, Methodology, Data curation. **Martin G. De Kauwe:** Writing – review & editing, Writing – original draft, Visualization, Methodology, Investigation, Formal analysis. **Sanaa Hobeichi:** Writing – review & editing, Methodology, Formal analysis. **Andy J. Pitman:** Writing – review & editing, Writing – original draft, Visualization, Supervision, Project administration, Methodology, Investigation, Funding acquisition, Formal analysis, Conceptualization.

## Declaration of competing interest

The authors declare that they have no known competing financial interests or personal relationships that could have appeared to influence the work reported in this paper.

## Data availability

Data will be made available on request.

## Acknowledgements

This research was supported by the ARC Centre of Excellence for Climate Extremes (CE170100023). This research/project was undertaken with the assistance of resources and services from the National Computational Infrastructure (NCI), which is supported by the Australian Government. AMU is supported by the Australian Research Council Discovery Early Career Researcher Award (DE200100086). MEBS acknowledges support from an ARC Discovery Grant (DP190101823). MGDK acknowledges funding from the UK Natural Environment Research Council (NE/W010003/1).

## Appendix A. Supplementary data

Supplementary data to this article can be found online at https://doi.org/10.1016/j.wace.2024.100703.

## References

Abram, N.J., Henley, B.J., Sen Gupta, A., Lippmann, T.J.R.R., Clarke, H., Dowdy, A.J., Sharples, J.J., Nolan, R.H., Zhang, T., Wooster, M.J., Wurtzel, J.B., Meissner, K.J., Pitman, A.J., Ukkola, A.M., Murphy, B.P., Tapper, N.J., Boer, M.M., 2021. Connections of climate change and variability to large and extreme forest fires in southeast Australia. Communications Earth & Environment 2, 8. https://doi.org/10.1038/s43247-020-00065-8.

Ajjur, S.B., Al-Ghamdi, S.G., 2021. Global hotspots for future absolute temperature extremes from CMIP6 models. Earth Space Sci. 8 https://doi.org/10.1029/2021EA001817.

Alessandri, A., Catalano, F., De Felice, M., Van Den Hurk, B., Doblas Reyes, F., Boussetta, S., Balsamo, G., Miller, P.A., 2017. Multi-scale enhancement of climate prediction over land by increasing the model sensitivity to vegetation variability in EC-Earth. Clim. Dynam. 49, 1215–1237. https://doi.org/10.1007/s00382-016-3372-4.

Biudes, M.S., Machado, N.G., Danelichen, V.H. de M., Souza, M.C., Vourlitis, G.L., Nogueira, J. de S., 2014. Ground and remote sensing-based measurements of leaf area index in a transitional forest and seasonal flooded forest in Brazil. Int. J. Biometeorol. 58, 1181–1193. https://doi.org/10.1007/s00484-013-0713-4.

Boer, M.M., Resco de Dios, V., Bradstock, R.A., 2020. Unprecedented burn area of Australian mega forest fires. Nat. Clim. Change 10, 171–172. https://doi.org/10.1038/s41558-020-0716-1.

Boschetti, L., Roy, D.P., Giglio, L., Huang, H., Zubkova, M., Humber, M.L., 2019. Global validation of the collection 6 MODIS burned area product. Rem. Sens. Environ. 235 https://doi.org/10.1016/j.rse.2019.111490.

Boussetta, S., Balsamo, G., Beljaars, A., Kral, T., Jarlan, L., 2013. Impact of a satellite-derived leaf area index monthly climatology in a global numerical weather prediction model. Int. J. Rem. Sens. 34, 3520–3542. https://doi.org/10.1080/01431161.2012.716543.

Boussetta, S., Balsamo, G., Dutra, E., Beljaars, A., Albergel, C., 2015. Assimilation of surface albedo and vegetation states from satellite observations and their impact on numerical weather prediction. Rem. Sens. Environ. 163, 111–126. https://doi.org/10.1016/j.rse.2015.03.009.

Boyer, J.S., Byrne, P., Cassman, K.G., Cooper, M., Delmer, D., Greene, T., Gruis, F., Habben, J., Hausmann, N., Kenny, N., Lafitte, R., Paszkiewicz, S., Porter, D., Schlegel, A., Schussler, J., Setter, T., Shanahan, J., Sharp, R.E., Vyn, T.J., Warner, D., Gaffney, J., 2013. The U.S. drought of 2012 in perspective: a call to action. Global Food Secur. 2, 139–143. https://doi.org/10.1016/j.gfs.2013.08.002.

Bréda, N., Huc, R., Granier, A., Dreyer, E., 2006. Temperate forest trees and stands under severe drought: a review of ecophysiological responses, adaptation processes and long-term consequences. Ann. For. Sci. 63, 625–644.

Bureau of Meteorology, 2020a. Special Climate Statement 70 Update-Drought Conditions in Australia and Impact on Water Resources in the Murray-Darling Basin.

Bureau of Meteorology, 2020b. Special Climate Statement 73—extreme Heat and Fire Weather in December 2019 and January 2020.

Bureau of Meteorology, 2019. Special Climate Statement 68-widespread Heatwaves during December 2018 and January 2019.

Byrne, B., Liu, J., Lee, M., Yin, Y., Bowman, K.W., Miyazaki, K., Norton, A.J., Joiner, J., Pollard, D.F., Griffith, D.W.T., Velazco, V.A., Deutscher, N.M., Jones, N.B., Paton-Walsh, C., 2021. The carbon cycle of southeastsoutheast Australia during 2019–2020: drought, fires, and subsequent recovery. AGU Advances 2. https://doi.org/10.1029/2021av000469.

Chiodi, A.M., Potter, B.E., Larkin, N.K., 2021. Multi-decadal change in western US nighttime vapor pressure deficit. Geophys. Res. Lett. 48 https://doi.org/10.1029/2021GL092830.

Cosby, B.J., Hornberger, G.M., Clapp, R.B., Ginn, T.R., 1984. A statistical exploration of the relationships of soil moisture characteristics to the physical properties of soils. Water Resour. Res. 20, 682–690. https://doi.org/10.1029/WR020i006p00682.

De Kauwe, M.G., Medlyn, B.E., Ukkola, A.M., Mu, M., Sabot, M.E.B., Pitman, A.J., Meir, P., Cernusak, L.A., Rifai, S.W., Choat, B., Tissue, D.T., Blackman, C.J., Li, X., Roderick, M., Briggs, P.R., 2020. Identifying areas at risk of drought-induced tree mortality across South-Eastern Australia. Global Change Biol. 26, 5716–5733. https://doi.org/10.1111/gcb.15215.

De Kauwe, M.G., Sabot, M.E.B., Medlyn, B.E., Pitman, A.J., Meir, P., Cernusak, L.A., Gallagher, R.V., Ukkola, A.M., Rifai, S.W., Choat, B., 2022. Towards species-level forecasts of drought-induced tree mortality risk. New Phytol. https://doi.org/10.1111/nph.18129.

Deb, P., Moradkhani, H., Abbaszadeh, P., Kiem, A.S., Engström, J., Keellings, D., Sharma, A., 2020. Causes of the widespread 2019–2020 Australian bushfire season. Earth's Future 8. https://doi.org/10.1029/2020EF001671.

Decker, M., 2015. Development and evaluation of a new soil moisture and runoff parameterization for the CABLE LSM including subgrid-scale processes. J. Adv. Model. Earth Syst. 7, 1788–1809. https://doi.org/10.1002/2015MS000507.

Decker, M., Or, D., Pitman, A., Ukkola, A., 2017. New turbulent resistance parameterization for soil evaporation based on a pore-scale model: impact on surface fluxes in CABLE. J. Adv. Model. Earth Syst. 9, 220–238. https://doi.org/10.1002/2016MS000832.

Dirmeyer, P.A., Halder, S., 2016. Sensitivity of numerical weather forecasts to initial soil moisture variations in CFSv2. Weather Forecast. https://doi.org/10.1175/WAF-D-16-0049.1.
Dobos, E., 2005. Albedo. In: Encyclopedia of Soil Science - Two-Volume Set. CRC Press.
Duveiller, G., Hooker, J., Cescatti, A., 2018. The mark of vegetation change on Earth's surface energy balance. Nat. Commun. 9, 679. https://doi.org/10.1038/s41467-017-02810-8.
Duveiller, G., Pickering, M., Muñoz-Sabater, J., Caporaso, L., Boussetta, S., Balsamo, G., Cescatti, A., 2023. Getting the leaves right matters for estimating temperature extremes. Geosci. Model Dev. (GMD) 16, 7357–7373. https://doi.org/10.5194/gmd-16-7357-2023.
Dy, C.Y., Fung, J.C.H., 2016. Updated global soil map for the Weather Research and Forecasting model and soil moisture initialization for the Noah land surface model. J. Geophys. Res. 121, 8777–8800. https://doi.org/10.1002/2015JD024558.
Evans, J.P., Meng, X., McCabe, M.F., 2017. Land surface albedo and vegetation feedbacks enhanced the millennium drought in south-east Australia. Hydrol. Earth Syst. Sci. 21, 409–422. https://doi.org/10.5194/hess-21-409-2017.
Fang, H., Baret, F., Plummer, S., Schaepman-Strub, G., 2019. An overview of global leaf area index (LAI): methods, products, validation, and applications. Rev. Geophys. 57, 739–799. https://doi.org/10.1029/2018RG000608.
Fang, Z., Zhang, W., Brandt, M., Abdi, A.M., Fensholt, R., 2022. Globally increasing atmospheric aridity over the 21st century. Earth's Future 10. https://doi.org/10.1029/2022EF003019.
Filkov, A.I., Ngo, T., Matthews, S., Telfer, S., Penman, T.D., 2020. Impact of Australia's catastrophic 2019/20 bushfire season on communities and environment. Retrospective analysis and current trends. Journal of Safety Science and Resilience 1, 44–56. https://doi.org/10.1016/j.jnlssr.2020.06.009.
Forzieri, G., Miralles, D.G., Ciais, P., Alkama, R., Ryu, Y., Duveiller, G., Zhang, K., Robertson, E., Kautz, M., Martens, B., Jiang, C., Arneth, A., Georgievski, G., Li, W., Ceccherini, G., Anthoni, P., Lawrence, P., Wiltshire, A., Pongratz, J., Piao, S., Sitch, S., Goll, D.S., Arora, V.K., Lienert, S., Lombardozzi, D., Kato, E., Nabel, J.E.M. S., Tian, H., Friedlingstein, P., Cescatti, A., 2020. Increased control of vegetation on global terrestrial energy fluxes. Nat. Clim. Change. https://doi.org/10.1038/s41558-020-0717-0.
Giglio, L., Boschetti, L., Roy, D.P., Humber, M.L., Justice, C.O., 2018. The Collection 6 MODIS burned area mapping algorithm and product. Rem. Sens. Environ. 217, 72–85. https://doi.org/10.1016/j.rse.2018.08.005.
Graf, A., Wohlfahrt, G., Aranda-Barranco, S., Arriga, N., Brümmer, C., Ceschia, E., Ciais, P., Desai, A.R., Di Lonardo, S., Gharun, M., Grünwald, T., Hörtnagl, L., Kasak, K., Klosterhalfen, A., Knohl, A., Kowalska, N., Leuchner, M., Lindroth, A., Mauder, M., Migliavacca, M., Morel, A.C., Pfennig, A., Poorter, H., Terán, C.P., Reitz, O., Rebmann, C., Sanchez-Azofeifa, A., Schmidt, M., Šigut, L., Tomelleri, E., Yu, K., Varlagin, A., Vereecken, H., 2023. Joint optimization of land carbon uptake and albedo can help achieve moderate instantaneous and long-term cooling effects. Communications Earth and Environment 4. https://doi.org/10.1038/s43247-023-00958-4.
Gupta, A., Rico-Medina, A., Caño-Delgado, A.I., 2020. The physiology of plant responses to drought. Science 368, 266–269. https://doi.org/10.1126/science.aaz7614.
Hengl, T., Mendes de Jesus, J., Heuvelink, G.B.M., Ruiperez Gonzalez, M., Kilibarda, M., Blagotić, A., Shangguan, W., Wright, M.N., Geng, X., Bauer-Marschallinger, B., Guevara, M.A., Vargas, R., MacMillan, R.A., Batjes, N.H., Leenaars, J.G.B., Ribeiro, E., Wheeler, I., Mantel, S., Kempen, B., 2017. SoilGrids250m: global gridded soil information based on machine learning. PLoS One 12, e0169748. https://doi.org/10.1371/journal.pone.0169748.
Hersbach, H., Bell, B., Berrisford, P., Hirahara, S., Horányi, A., Muñoz-Sabater, J., Nicolas, J., Peubey, C., Radu, R., Schepers, D., Simmons, A., Soci, C., Abdalla, S., Abellan, X., Balsamo, G., Bechtold, P., Biavati, G., Bidlot, J., Bonavita, M., De Chiara, G., Dahlgren, P., Dee, D., Diamantakis, M., Dragani, R., Flemming, J., Forbes, R., Fuentes, M., Geer, A., Haimberger, L., Healy, S., Hogan, R.J., Hólm, E., Janisková, M., Keeley, S., Laloyaux, P., Lopez, P., Lupu, C., Radnoti, G., de Rosnay, P., Rozum, I., Vamborg, F., Villaume, S., Thépaut, J.N., 2020. The ERA5 global reanalysis. Q. J. R. Meteorol. Soc. 146, 1999–2049. https://doi.org/10.1002/qj.3803.
Hill, M.J., Senarath, U., Lee, A., Zeppel, M., Nightingale, J.M., Williams, R. (Dick) J., McVicar, T.R., 2006. Assessment of the MODIS LAI product for Australian ecosystems. Rem. Sens. Environ. 101, 495–518. https://doi.org/10.1016/j.rse.2006.01.010.
Hirsch, A.L., Evans, J.P., Di Virgilio, G., Perkins-Kirkpatrick, S.E., Argüeso, D., Pitman, A. J., Carouge, C.C., Kala, J., Andrys, J., Petrelli, P., Rockel, B., 2019a. Amplification of Australian heatwaves via local land-atmosphere coupling. J. Geophys. Res. Atmos. 124, 13625–13647. https://doi.org/10.1029/2019JD030665.
Hirsch, A.L., Kala, J., Carouge, C.C., De Kauwe, M.G., Di Virgilio, G., Ukkola, A.M., Evans, J.P., Abramowitz, G., 2019b. Evaluation of the CABLEv2.3.4 land surface model coupled to NU-WRFv3.9.1.1 in simulating temperature and precipitation means and extremes over CORDEX AustralAsia within a WRF physics ensemble. J. Adv. Model. Earth Syst. 11, 4466–4488. https://doi.org/10.1029/2019MS001845.
Hirsch, A.L., King, M.J., 2020. Atmospheric and land surface contributions to heatwaves: an Australian perspective. J. Geophys. Res. Atmos. 125 https://doi.org/10.1029/2020JD033223.
Jiao, T., Williams, C.A., Rogan, J., De Kauwe, M.G., Medlyn, B.E., 2020. Drought impacts on Australian vegetation during the millennium drought measured with multisource spaceborne remote sensing. J. Geophys. Res.: Biogeosciences 125, e2019JG005145.
Jones, D., Wang, W., Fawcett, R., 2009. High-quality spatial climate data-sets for Australia. Australian Meteorological and Oceanographic Journal 58, 233–248. https://doi.org/10.22499/2.5804.003.
King, A.D., Pitman, A.J., Henley, B.J., Ukkola, A.M., Brown, J.R., 2020. The role of climate variability in Australian drought. Nat. Clim. Change 10, 177–179. https://doi.org/10.1038/s41558-020-0718-z.
Knote, C., Bonafe, G., Giuseppe, F.D., 2009. Leaf area index specification for use in mesoscale weather prediction systems. Mon. Weather Rev. 137 (1), 3535–3550. https://doi.org/10.1175/2009MWR2891.
Koster, R.D., Walker, G.K., 2015. Interactive vegetation phenology, soil moisture, and monthly temperature forecasts. J. Hydrometeorol. 16, 1456–1465. https://doi.org/10.1175/JHM-D-14-0205.1.
Launiainen, S., Guan, M., Salmivaara, A., Kieloaho, A.J., 2019. Modeling boreal forest evapotranspiration and water balance at stand and catchment scales: a spatial approach. Hydrol. Earth Syst. Sci. 23, 3457–3480. https://doi.org/10.5194/hess-23-3457-2019.
Leuning, R., Cleugh, H.A., Zeglin, S.J., Hughes, D., 2005. Carbon and water fluxes over a temperate Eucalyptus forest and tropical wet/dry savanna in Australia: measurements and comparison with MODIS remote sensing estimates. Agric. For. Meteorol. 129, 153–173.
Li, Y., Zhao, M., Motesharrei, S., Mu, Q., Kalnay, E., Li, S., 2015. Local cooling and warming effects of forests based on satellite observations. Nat. Commun. 6 https://doi.org/10.1038/ncomms7603.
Liu, C., Chen, Y.D., 2024. Impacts of vegetation dynamics on hydrological simulations under drought conditions in a humid river basin in Southern China. Ecohydrology 17, e2630. https://doi.org/10.1002/eco.2630.
Mayr, M.J., Samimi, C., 2015. Comparing the dry season in-situ leaf area index (LAI) derived from high-resolution RapidEye imagery with MODIS LAI in a Namibian savanna. Rem. Sens. 7, 4834–4857. https://doi.org/10.3390/rs70404834.
Meng, X.H., Evans, J.P., McCabe, M.F., 2014a. The impact of observed vegetation changes on land–atmosphere feedbacks during drought. J. Hydrometeorol. 15, 759–776. https://doi.org/10.1175/JHM-D-13-0130.1.
Meng, X.H., Evans, J.P., McCabe, M.F., 2014b. The influence of inter-annually varying albedo on regional climate and drought. Clim. Dynam. 42, 787–803. https://doi.org/10.1007/s00382-013-1790-0.
Miralles, D.G., Gentine, P., Seneviratne, S.I., Teuling, A.J., 2019. Land-atmospheric feedbacks during droughts and heatwaves: state of the science and current challenges. Ann. N. Y. Acad. Sci. 1436, 19–35. https://doi.org/10.1111/nyas.13912.
Miralles, D.G., Teuling, A.J., van Heerwaarden, C.C., De Arellano, J.V.G., Vilà-Guerau de Arellano, J., De Arellano, J.V.G., Vilà-Guerau de Arellano, J., 2014. Mega-heatwave temperatures due to combined soil desiccation and atmospheric heat accumulation. Nat. Geosci. 7, 345–349. https://doi.org/10.1038/ngeo2141.
Mu, M., De Kauwe, M.G., Ukkola, A.M., Pitman, A.J., Gimeno, T.E., Medlyn, B.E., Or, D., Yang, J., Ellsworth, D.S., 2021a. Evaluating a land surface model at a water-limited site: implications for land surface contributions to droughts and heatwaves. Hydrol. Earth Syst. Sci. 25, 447–471. https://doi.org/10.5194/hess-25-447-2021.
Mu, M., De Kauwe, M.G., Ukkola, A.M., Pitman, A.J., Guo, W., Hobeichi, S., Briggs, P.R., 2021b. Exploring how groundwater buffers the influence of heatwaves on vegetation function during multi-year droughts. Earth System Dynamics 12, 919–938. https://doi.org/10.5194/esd-12-919-2021.
Mu, M., Pitman, A.J., De Kauwe, M.G., Ukkola, A.M., Ge, J., 2022. How do groundwater dynamics influence heatwaves in southeast Australia? Weather Clim. Extrem. 37, 100479 https://doi.org/10.1016/j.wace.2022.100479.
Myneni, R., Knyazikhin, Y., Park, T., 2021. MODIS/Terra+Aqua leaf area index/FPAR 4-day L4 global 500m SIN grid V061. https://doi.org/10.5067/MODIS/MCD15A3H.061.
Nguyen, H., Wheeler, M.C., Hendon, H.H., Lim, E.-P., Otkin, J.A., 2021. The 2019 flash droughts in subtropical eastern Australia and their association with large-scale climate drivers. Weather Clim. Extrem. 32, 100321 https://doi.org/10.1016/j.wace.2021.100321.
Niu, G.Y., Fang, Y.H., Chang, L.L., Jin, J., Yuan, H., Zeng, X., 2020. Enhancing the noah-MP ecosystem response to droughts with an explicit representation of plant water storage supplied by dynamic root water uptake. J. Adv. Model. Earth Syst. 12 https://doi.org/10.1029/2020MS002062, 0–3.
Nogueira, M., Albergel, C., Boussetta, S., Johannsen, F., Trigo, I.F., Ermida, S.L., Martins, J.P.A., Dutra, E., 2020. Role of vegetation in representing land surface temperature in the CHTESSEL (CY45R1) and SURFEX-ISBA (v8.1) land surface models: a case study over Iberia. Geosci. Model Dev. (GMD) 13, 3975–3993. https://doi.org/10.5194/gmd-13-3975-2020.
Nolan, R.H., Gauthey, A., Losso, A., Medlyn, B.E., Smith, R., Chhajed, S.S., Fuller, K., Song, M., Li, X., Beaumont, L.J., Boer, M.M., Wright, I.J., Choat, B., 2021. Hydraulic failure and tree size linked with canopy die-back in eucalypt forest during extreme drought. New Phytol. 230, 1354–1365. https://doi.org/10.1111/nph.17298.
Nsw, D.P.I., 2020. NSW State Seasonal Update - December 2019.
Osman, M., Zaitchik, B.F., Winstead, N.S., 2022. Cascading drought-heat dynamics during the 2021 southwest United States heatwave. Geophys. Res. Lett. 49 https://doi.org/10.1029/2022GL099265.
Peters, W., van der Velde, I.R., van Schaik, E., Miller, J.B., Ciais, P., Duarte, H.F., van der Laan-Luijkx, I.T., van der Molen, M.K., Scholze, M., Schaefer, K., Vidale, P.L., Verhoef, A., Wårlind, D., Zhu, D., Tans, P.P., Vaughn, B., White, J.W.C., 2018. Increased water-use efficiency and reduced CO2uptake by plants during droughts at a continental scale. Nat. Geosci. 11, 744–748. https://doi.org/10.1038/s41561-018-0212-7.
Rasmijn, L.M., Van Der Schrier, G., Bintanja, R., Barkmeijer, J., Sterl, A., Hazeleger, W., 2018. Future equivalent of 2010 Russian heatwave intensified by weakening soil moisture constraints. Nat. Clim. Change 8, 381–385. https://doi.org/10.1038/s41558-018-0114-0.
Roach, J., 2020. Australia wildfire damages and losses to exceed $100 billion. AccuWeather estimates [WWW Document]. URL. https://www.accuweather.com

/en/business/australia-wildfire-economic-damages-and-losses-to-reach-110-billion/657235. (Accessed 11 January 2023).
Ruiz-Vásquez, M., O, S., Arduini, G., Boussetta, S., Brenning, A., Bastos, A., Koirala, S., Balsamo, G., Reichstein, M., Orth, R., 2023. Impact of updating vegetation information on land surface model performance. J. Geophys. Res. Atmos. 128, e2023JD039076 https://doi.org/10.1029/2023JD039076.
Ruiz-Vásquez, M., O, S., Brenning, A., Koster, R.D., Balsamo, G., Weber, U., Arduini, G., Bastos, A., Reichstein, M., Orth, R., 2022. Exploring the relationship between temperature forecast errors and Earth system variables. Earth System Dynamics 13, 1451–1471. https://doi.org/10.5194/esd-13-1451-2022.
Sabot, M.E.B.B., De Kauwe, M.G., Pitman, A.J., Medlyn, B.E., Verhoef, A., Ukkola, A.M., Abramowitz, G., 2020. Plant profit maximization improves predictions of European forest responses to drought. New Phytol. 226, 1638–1655. https://doi.org/10.1111/nph.16376.
Sabot, M.E.B., De Kauwe, M.G., Pitman, A.J., Ellsworth, D.S., Medlyn, B.E., Caldararu, S., Zaehle, S., Crous, K.Y., Gimeno, T.E., Wujeska-Klause, A., Mu, M., Yang, J., 2022. Predicting resilience through the lens of competing adjustments to vegetation function. Plant Cell Environ. https://doi.org/10.1111/pce.14376.
Sanderson, B.M., Fisher, R.A., 2020. A fiery wake-up call for climate science. Nat. Clim. Change 10, 175–177. https://doi.org/10.1038/s41558-020-0707-2.
Schaaf, C., Wang, Z., 2021. MODIS/Terra+Aqua BRDF/albedo albedo daily L3 global 0.05Deg CMG V061. https://doi.org/10.5067/MODIS/MCD43C3.061.
Schumacher, D.L., Keune, J., van Heerwaarden, C.C., Vilà-Guerau de Arellano, J., Teuling, A.J., Miralles, D.G., 2019. Amplification of mega-heatwaves through heat torrents fuelled by upwind drought. Nat. Geosci. 12, 712–717. https://doi.org/10.1038/s41561-019-0431-6.
Segura, R., Badia, A., Ventura, S., Gilabert, J., Martilli, A., Villalba, G., 2021. Sensitivity study of PBL schemes and soil initialization using the WRF-BEP-BEM model over a Mediterranean coastal city. Urban Clim. 39, 100982 https://doi.org/10.1016/j.uclim.2021.100982.
Seneviratne, S.I., Corti, T., Davin, E.L., Hirschi, M., Jaeger, E.B., Lehner, I., Orlowsky, B., Teuling, A.J., 2010. Investigating soil moisture–climate interactions in a changing climate: a review. Earth Sci. Rev. 99, 125–161. https://doi.org/10.1016/j.earscirev.2010.02.004.
Sharples, J.J., McRae, R.H.D., 2011. Evaluation of a very simple model for predicting the moisture content of eucalypt litter. Int. J. Wildland Fire 20, 1000–1005. https://doi.org/10.1071/WF11006.
Sooraj, K.P., Terray, P., Masson, S., Crétat, J., 2019. Modulations of the Indian summer monsoon by the hot subtropical deserts: insights from coupled sensitivity experiments. Clim. Dynam. 52, 4527–4555. https://doi.org/10.1007/s00382-018-4396-8.
Stahl, K., Kohn, I., Blauhut, V., Urquijo, J., De Stefano, L., Acácio, V., Dias, S., Stagge, J. H., Tallaksen, L.M., Kampragou, E., Van Loon, A.F., Barker, L.J., Melsen, L.A., Bifulco, C., Musolino, D., de Carli, A., Massarutto, A., Assimacopoulos, D., Van Lanen, H.A.J., 2016. Impacts of European drought events: insights from an international database of text-based reports. Nat. Hazards Earth Syst. Sci. 16, 801–819. https://doi.org/10.5194/nhess-16-801-2016.
Su, Y., Zhang, C., Ciais, P., Zeng, Z., Cescatti, A., Shang, J., Chen, J.M., Liu, J., Wang, Y. P., Yuan, W., Peng, S., Lee, X., Zhu, Z., Fan, L., Liu, X., Liu, L., Lafortezza, R., Li, Y., Ren, J., Yang, X., Chen, X., 2023. Asymmetric influence of forest cover gain and loss on land surface temperature. Nat. Clim. Change 13, 823–831. https://doi.org/10.1038/s41558-023-01757-7.
Sydney Water, 2020. Water Conservation Report 2019–2020, NSW State Seasonal Update - December 2019.
Tarek, M., Brissette, F.P., Arsenault, R., 2020. Evaluation of the ERA5 reanalysis as a potential reference dataset for hydrological modelling over North America. Hydrol. Earth Syst. Sci. 24, 2527–2544. https://doi.org/10.5194/hess-24-2527-2020.
Terray, P., Sooraj, K.P., Masson, S., Krishna, R.P.M., Samson, G., Prajeesh, A.G., 2018. Towards a realistic simulation of boreal summer tropical rainfall climatology in state-of-the-art coupled models: role of the background snow-free land albedo. Clim. Dynam. 50, 3413–3439. https://doi.org/10.1007/s00382-017-3812-9.
Ukkola, A.M., Pitman, A.J., Decker, M., De Kauwe, M.G., Abramowitz, G., Kala, J., Wang, Y.-P., 2016. Modelling evapotranspiration during precipitation deficits: identifying critical processes in a land surface model. Hydrol. Earth Syst. Sci. 20, 2403–2419. https://doi.org/10.5194/hess-20-2403-2016.
van Dijk, A.I., Beck, H.E., Crosbie, R.S., de Jeu, R.A.M.M., Liu, Y.Y., Podger, G.M., Timbal, B., Viney, N.R., 2013. The Millennium Drought in southeast Australia (2001-2009): Natural and human causes and implications for water resources, ecosystems, economy, and society. Water Resour. Res. 49, 1040–1057. https://doi.org/10.1002/wrcr.20123.
Wedd, R., Alves, O., De Burgh-Day, C., Down, C., Griffiths, M., Hendon, H.H., Hudson, D., Li, S., Lim, E.-P., Marshall, A.G., Shi, L., Smith, P., Smith, G., Spillman, C.M., Wang, G., Wheeler, M.C., Yan, H., Yin, Y., Young, G., Zhao, M., Xiao, Y., Zhou, X., 2022. ACCESS-S2: the upgraded Bureau of Meteorology multi-week to seasonal prediction system. J. South. Hemisph. Earth Syst. Sci. 72, 218–242. https://doi.org/10.1071/ES22026.
Wei, J., Zhao, J., Chen, H., Liang, X.Z., 2021. Coupling between land surface fluxes and lifting condensation level: mechanisms and sensitivity to model physics parameterizations. J. Geophys. Res. Atmos. 126 https://doi.org/10.1029/2020JD034313.
Wittwer, G., Waschik, R., 2021. Estimating the economic impacts of the 2017–2019 drought and 2019–2020 bushfires on regional NSW and the rest of Australia. Aust. J. Agric. Resour. Econ. 65, 918–936. https://doi.org/10.1111/1467-8489.12441.
Wu, X., Wang, L., Yao, R., Luo, M., Li, X., 2021. Identifying the dominant driving factors of heat waves in the North China Plain. Atmos. Res. 252, 105458 https://doi.org/10.1016/j.atmosres.2021.105458.
Yan, D., Liu, T., Dong, W., Liao, X., Luo, S., Wu, K., Zhu, X., Zheng, Z., Wen, X., 2020. Integrating remote sensing data with WRF model for improved 2-m temperature and humidity simulations in China. Dynam. Atmos. Oceans 89, 101127. https://doi.org/10.1016/j.dynatmoce.2019.101127.
Zhang, H., Liu, J., Li, H., Meng, X., Ablikim, A., 2020. The impacts of soil moisture initialization on the forecasts of weather research and forecasting model: a case study in Xinjiang. China. Water (Switzerland) 12, 1–16. https://doi.org/10.3390/w12071892.
Zscheischler, J., Naveau, P., Martius, O., Engelke, S., Raible, C.C., 2021. Evaluating the dependence structure of compound precipitation and wind speed extremes. Earth System Dynamics 12, 1–16. https://doi.org/10.5194/esd-12-1-2021.